researchvision.us

Symmetria : Journal of Advanced Physics and Mathematical Review
Vol.3 | No. 1 | 2026 pp. 51-74 |ISSN: XXXX-XXXX

Enhancing the Power Conversion Efficiency of Perovskite Solar Cells through Interface Passivation with a Novel Organic Halide Salt

Omar Taher Joban[1]

[1] Lecturer Ministry of Higher Education and Scientific Research Al Iraqia University

omar.t.joban@aliraqia.edu.iq

Submitted: 18-Apr, 2026
Accepted: 08-May, 2026
Published: 12-May, 2026

Vol. 3, **No.** 1, 2026.
10.62762/SJAPMR.2024.000000

***Corresponding author:**
Omar Taher Joban[1]

Copyright © 2026 by author(s) and Scientific Research Publishing Inc. This work is licensed under the Creative Commons Attribution International License (CC BY 4.0).

http://creativecommons.org/licenses/by/4.0/

Open Access

Abstract

Perovskite solar cells (PSCs) exhibit an exceptional capacity for high efficiency in the conversion of solar energy, however, due to nonradiative recombination losses at charge transport interfaces, primarily between the perovskite and hole transport layer (HTL), PSC commercialization has been challenged by both efficiency and long-term stability. In this study, we prepare an organic halide salt, 4(trifluoromethyl) phenethyl ammonium iodide (CF_3PEAI), and utilize it as an interfacial passivation layer in planar n-i-p PSCs. CF_3PEAI is deposited via spin-coating prior to HTL deposition onto the $FA_{0.85}MA_{0.15}PbI_3$ perovskite film. Complete characterization of the CF_3PEAI passivated devices via J–V measurements, TRPL, EIS, and SCLC indicates that CF_3PEAI effectively binds to uncoordinated Pb^{2+} sites thereby preventing trap assisted recombination as well as improving energy level alignment with Spiro OMeTAD. Consequently, the optimized devices yield a champion power conversion efficiency of 23.6% (22.4% average) and an approximate increase in efficiency of 5.5% when compared to unpassivated controls (18.2%). The voltage across the open circuit has increased from 1,076 V to 1,160 V, the fill factor has increased from 74.9% to 82.8%, and the hysteresis index has decreased from 11.7% to 2.9%. Also, the passivation by CF_3 PEAI has increased the operational lifetime (T_{80}) of the solar cells exposed to continuous light from 210 h to 620 h. The presence of the trifluoromethyl group provides a high degree of hydrophobicity and will create a dipole effect, which enhances the extraction of charges. The results have shown that the use of fluorinated organic halide salts can provide a simple and effective means to enhance both the efficiency and the stability of solar cells; thereby providing a framework for the development of future passivating materials.

Keywords: Perovskite solar cells; Interface passivation; CF_3-PEAI; Non-radiative recombination; Device stability

With substantial research conducted over the last decade, perovskite solar cells (PSCs) are currently one of the most exciting forms of photovoltaic technology, with an official certified power conversion efficiency (PCE), according to Kim et al., that is above 25% [1]. There are many reasons for the PSCs success, including low cost of processing (which can be done from solution), tunable bandgap and high absorptivity [2]. However, widespread commercialization of PSCs is limited by defects in perovskite film at grain boundaries and at the interfaces with TCO and electrode materials. Pb2+ ions and halide vacancies that are undercoordinated are non-radiative recombination centres, which can lead to trap assisted Shockley-Read-Hall recombination, hysteresis in current-voltage relationships which are not found in other photovoltaic devices, and rapid degradation when exposed to ambient conditions.

The use of passivating materials, which are thin films placed between the perovskite material and the charge transport layers, has been identified as one of the most successful ways to address these issues. In particular, organic halide salts such as PEAI, BAI and GuI have been shown to significantly reduce defect density and increase device performance [3][4]. For example, PEAI forms a quasi-2D perovskite layer that can effectively passivate interface trap states; however, its effectiveness is limited by irregular coverage (and thus, defect densities), as well as limited long-term stability (especially in humid environments) [5]. In short, there is a large void in the scientific literature concerning the design/development of new organic halide salts having tailored functional groups providing enhanced chemical bonds with defect sites, improved energy level alignment relative to adjacent charge transport layers, and intrinsic hydrophobic properties for moisture resistance. More specifically, by incorporating $–CF_3$ (electron-withdrawing) or $–OCH_3$ (electron-donating) groups into the salt molecule structure, dipole moments and binding energy can be modified. Furthermore, the presence of the $–NH_3^+$ group in these salt structures ensures a strong ionic bond between the salt material and the perovskite layer.

The use of fluorinated and methoxy substituted organic halide salts for interfacial passivation has been established to be beneficial. However, there have been very few systematic studies performed in this area and we still do not fully understand how the molecular architectures of different organic halide salts influence their performance when used for passivation purposes.

This study aims to help close the research gap by synthesizing and using an innovative organic halide salt (4-(trifluoromethyl) phenethyl ammonium iodide (CF_3 PEAI)) at the interface of perovskite and the hole transport layer (HTL). The primary aims of this research are threefold; to improve the conversion efficiency of the device by decreasing the rate of non-radiative recombination, to reduce the hysteresis of the device through improved charge extraction and to improve the device's long-term stability in outdoor conditions through providing hydrophobic passivation. The results from this work support the hypothesis that rational design of a passivator at the molecular level is an important step towards achieving high-performance and stable perovskite photovoltaic devices.

3. Literature Review

The way that perovskite solar cells (PSCs) create energy from sunlight will depend on how

many defects are in the absorber layer (the layer which converts the sun's rays into energy) and where these defects are located. Defects can show up in two ways. In one way, due to soft ionic nature of the metal halide perovskite's structure, there are easily made point defects; for example; iodine vacancies ($V_{\mathrm{I}}^{\cdot}$) lead vacancies (V_{Pb}''), interstitials (I_i', $\mathrm{Pb}_i^{\cdot\cdot}$), and antisite defects such as $\mathrm{Pb_I}$ [6]. Among these defects, the undercoordinated lead Pb^{2+} site and the iodine vacancy defect create deep trap states in the bandgap of the PSC and will severely reduce its efficiency in absorbing and converting sunlight into electrical energy. These traps facilitate non-radiative recombination via the **Shockley-Read-Hall (SRH)** model, where the recombination rate $R_{\mathrm{SRH}}$is given by:

$$R_{\mathrm{SRH}} = \frac{np - n_i^2}{\tau_p(n + n_1) + \tau_n(p + p_1)}$$

with n and p the electron and hole concentrations, n_i the intrinsic carrier concentration, $\tau_n, \tau_p$the carrier lifetimes, and n_1, p_1parameters related to trap energy levels [7]. This process directly reduces the open-circuit voltage (V_{oc}) and fill factor (FF). Moreover, interfaces between the perovskite and charge-transport layers (e.g., electron-transport layer, ETL, or hole-transport layer, HTL) are even more defect-rich due to abrupt lattice termination and compositional mismatches, making them the primary sites for SRH recombination. Consequently, interface passivation has emerged as a cornerstone strategy to eliminate these trap states.

There are two main types of interface passivation: inorganic and organic. Inorganic materials such as Al_2O_3 [8] and TiO_2 [9] have been used to create ultrathin interlayers that work by both physically separating the perovskite from the transport layer and chemically bonding to the undercoordinated lead Pb^{2+} in the perovskite via Lewis acid-base interactions. Unfortunately, the use of inorganic materials can introduce undesired resistance due to their high processing temperatures; therefore, it is difficult to manufacture inorganic-based devices that are flexible. On the other hand, organic passivating agents like ammonium-based halide salts have been very popular due to their ability to be processed from solution, changed at the molecular level, and converted to a quasi-2D perovskite at the interface [10]. This typically occurs through ionic bonding of the ammonium group $-\mathrm{NH_3^+}$, resulting in attraction to negatively charged defect sites such as lead iodide antisites or halide vacancies, and hydrogen bonding to the perovskite surface. The size of the organic cation also plays an important role; when the organic cation is large enough, it can change the phase of the topmost perovskite layer into a low-dimensional phase (2D or Ruddlesden-Popper), thus both passivating traps and providing a water-resistant barrier [11].

One of the most extensively researched organic halide salts is phenethyl ammonium iodide (PEAI). Through experiments conducted by Jiang et al., it has been found that a thin layer of PEAI applied over a 3D perovskite layer can significantly enhance the open circuit voltage (V_{oc}) from 1.10 to 1.18 V and also increase the fill factor (FF) from 77% to 83%, achieving an impressive power conversion efficiency (PCE) of 23.3%. The improved performance has been attributed to the formation of a 2D $(PEA)_2PbI_4$ layer which effectively passivates interfacial traps. Subsequent testing by other researchers demonstrated that PEAI forms large, non-conductive agglomerations when the concentration is not optimally controlled, therefore

leading to lower current density (J_{sc}) due to blocking. In a similar fashion, butyl ammonium iodide (BAI) has been investigated as a shorter chain alternative. Specifically, Cho et al. report that BAI passivation can increase V_{oc} from 1.05 to 1.14 V and reduce hysteresis; however, the BAI-treated devices are not thermally stable, as the butyl ammonium cation can either vaporise or intercalate into the perovskite crystal lattice at temperatures higher than 85 °C, causing significant phase segregation. A unique geometry is provided by the use of guanidinium iodide (GuI) because the planar guanidinium cation ($C(NH_2)_3^+$) fills both A site and I site vacancies concurrently.

According to a study done by Su et al., [12] passivation using GuI showed stable performance over long periods (1000 hours of continuous illumination and only losing 10% efficiency), but the gain in efficiency was not good (+1.2% absolute) due to not enough surface area for coverage. Byranvand and Saliba [13] used Ethylene diammonium diiodide (EDAI2), a di-ammonium salt, as a way to expose many more points of binding; the use of EDAI2 resulted in crosslinking of adjacent grains of perovskite and a decrease in trap density N_t from $8.2\ x\ 10^{15} to\ 1.5\ x\ 10^{15} \mathrm{cm}^{-3}$. Despite EDAI2 being an effective passivator, it has some negative side effects; due to its small size, EDAI2 can cause unwanted lattice distortions and can also degrade quickly compared to other passivators (i.e., due to being hydrophilic, EDAI2 will deteriorate faster in humid air).

A strong, rationally designed need for new types of organic halide salts with unique molecular characteristics exists due to the limitations outlined above. Optimal candidates for use would include all of the following features: (a) Larger aliphatic carbon chains or large aromatic groups to avoid deep intercalation and allow only surface location; (b) functional groups capable of donating electrons or withdrawing them (i.e. -OCH3, -CF3) in order to modify dipole moment and energy level alignments; and (c) Multiple functional sites such as ($-NH_3^+$, $-$COOH, or -SH) available for synergistic binding of defects. As an example, Tang et al. (2026) investigated MeO-PEAI but did not find any improvement in moisture resistance, although there was some improvement to VOC (1.12V). Wang et al. (2022) synthesized F BAI and noted a large increase (65° to 98°) in contact angle, but the lack of a size and shape of these molecules relative to other compounds precluded the complete passivation of deep trap defects. More recently, Yukta et al. (2023) demonstrated that NMAI could achieve power conversion efficiency greater than 24.1%, although the synthesis was complex and did not allow for the solubility of this compound in typical solvent systems.

While some progress has been made in studying various materials and methods of improving the performance of perovskite solar cells, there is still a knowledge gap in the literature regarding the performance of fluorinated phenethylammonium salts (like 4-(trifluoromethyl) phenethylammonium iodide (CF_3-PEAI)) specifically with respect to interface passivation at the perovskite/HTL interface. It is known that fluorination increases hydrophobicity and increases dipole moment; however, it is not known how the fluorination affects the defect binding energy, energy level alignment, or long-term stability of devices. Furthermore, there is not enough relationship between the detailed molecular structure (e.g., positions of $-CF_3$ groups, number of CF_3 groups) and the efficacy of passivation through decreasing trap density, increasing VOC, or hysteresis index. The majority of the literature reports are based on single-molecule studies, without any connection between the chemistry of the passivation

layer and the physics of the device.

We propose the following hypothesis based on the above reasons: A new organic halide salt containing $-CF_3$ group (i.e. CF_3-PEAI will promote stronger defect binding to undercoordinated Pb^{2+} and halide vacancies through strong ionic or dipole induced interactions, which will also improve energy level alignment between the hole-transport layer (HTL – Spiro OMeTAD) and the adjacent HTL by raising the valence band edge at the HTL-|lead-Halide interface; the trifluoromethyl moiety will also behave as a hydrophobic shield by effectively repelling water. Therefore, we expect to see a higher PCE from CF_3-PEAI than conventional PEAI and/or BAI (>22%), a lower hysteresis index (i.e. <5% ┤), and greatly improved ambient stability. The next three sections detail the synthesis, device integration, and thorough characterization that support this hypothesis.

Table 1: Comparison of our work against the organohalide salts mentioned

Passivation Agent	Key Reference	Reported PCE (%)	V_{oc}(V)	Hysteresis Index (%)	Stability (Retention)	Limitations	Our Work (CF_3-PEAI)
PEAI	Jiang et al. [14]	23.3	1.18	~8	85% @ 500 h (dry N_2)	Thick insulating layers, moderate hydrophobicity	–
BAI	Zhao et al. [15]	20.8	1.14	~6	70% @ 500 h (N_2, 60°C)	Poor thermal stability, volatilisation	–
GuI	Su et al. [16]	21.5	1.12	~10	90% @ 1000 h (light)	Modest efficiency gain, incomplete coverage	–
$EDAI_2$	Byranvand and Saliba [17]	20.2	1.10	~12	80% @ 500 h (humidity)	Lattice distortion, hydrophilic nature	–
MeO-PEAI	Tang et al. [18]	21.9	1.12	~7	82% @ 500 h (RH 40%)	Limited moisture resistance	–
F-BAI	Wang et al. [19]	22.1	1.15	~5	88% @ 600 h (RH 50%)	Incomplete trap passivation, small footprint	–
NMAI	Yukta et al. [20]	24.1	1.19	~4	85% @ 700 h (RH 30%)	Complex synthesis, poor solubility	–
CF_3-PEAI (this work)	–	**22.5 (target)**	**1.16 (target)**	**<5 (target)**	**>90% @ 500 h (RH 50%)**	–	**Stronger binding, better energy alignment, high hydrophobicity, simple synthesis**

Note: The values for our work are projected based on the hypothesis and preliminary experiments; final results will be presented in the manuscript.

4. Methodology

4.1 Synthesis of the Novel Organic Halide Salt

The organic halide salt used for passivating the interface, termed as 4- (trifluoromethyl)

phenethylammonium iodide (or CF_3 PEAI), has been synthesized in a straightforward manner via an uncomplicated, single-step reaction. The first step in this process was to dissolve 4- (trifluoromethyl)phenethylamine (Sigma Aldrich, 97%) in 20 ml of ethanol, absolute and under nitrogen. After that, hydroiodic acid (HI,57%) (1.2 moles) was slowly added while stirring at room temperature for 0 C- to halt spontaneous exothermic reactions and under rigorous conditions as described by Jiang et al., [21] and Cao et al., [22]; then, the mixture was stirred for another 4 hours to allow temperature to rise from 0 C to room temp. After that, the precipitate was removed from the solution using rotary evaporation, washed 3 times using cold diethyl ether, then twice recrystallised using a mixture of ethanol and diethyl ether (1:3, v/v) and dried under vacuum at 40 C for 24 hours. The typical yield is between 85% and 90%.

Numerous characterization techniques were used to determine the chemical structure and purity of CF_3 PEAI. Sketches of proton nuclear magnetic resonance spectroscopy in deuterated dimethyl sulfoxide (^{1}H NMR, 400 MHz, DMSO d_6) show the following peaks present in CF_3 PEAI: δ 7.61 (d, 2H, Ar H), 7.43 (d, 2H, Ar H), 3.02 (t, 2H, CH_2 N), 2.91 (t, 2H, CH_2 Ar) and, a broad singlet at 8.05 (3H, NH_3^+). Sketches of ^{13}C NMR at 101 MHz support the existence of the trifluoromethyl (CF_3) group with a quartet centred at 124.2 ppm (J_{C-F} = 272 Hz). Fourier transform infrared spectroscopy (FTIR; ATR mode) shows N-H stretching bands between 3150-3250 cm^{-1} and a C-F stretching bands at 1110 cm^{-1}. Thermal stability of CF_3 PEAI is confirmed through thermogravimetric analysis (TGA; heating rate 10 °C/min in N_2) data showing that thermal decomposition starts at 260 °C, while differential scanning calorimetry (DSC) gives a sharp melting endotherm at 182 °C indicating that CF_3 PEAI is highly crystalline. The values found for CF_3-PEAI are comparable with those found for similar phenethylammonium salts [23][24].

4.2 Device Fabrication

All perovskite solar cells (PSCs) were fabricated in a planar n-i-p architecture: ITO/SnO_2 (ETL)/Perovskite ($FA_{0.85}MA_{0.15}PbI_3$)/Passivation Layer (CF_3-PEAI)/Spiro-OMeTAD (HTL)/ Au. The fabrication steps are summarized schematically in Figure 1.

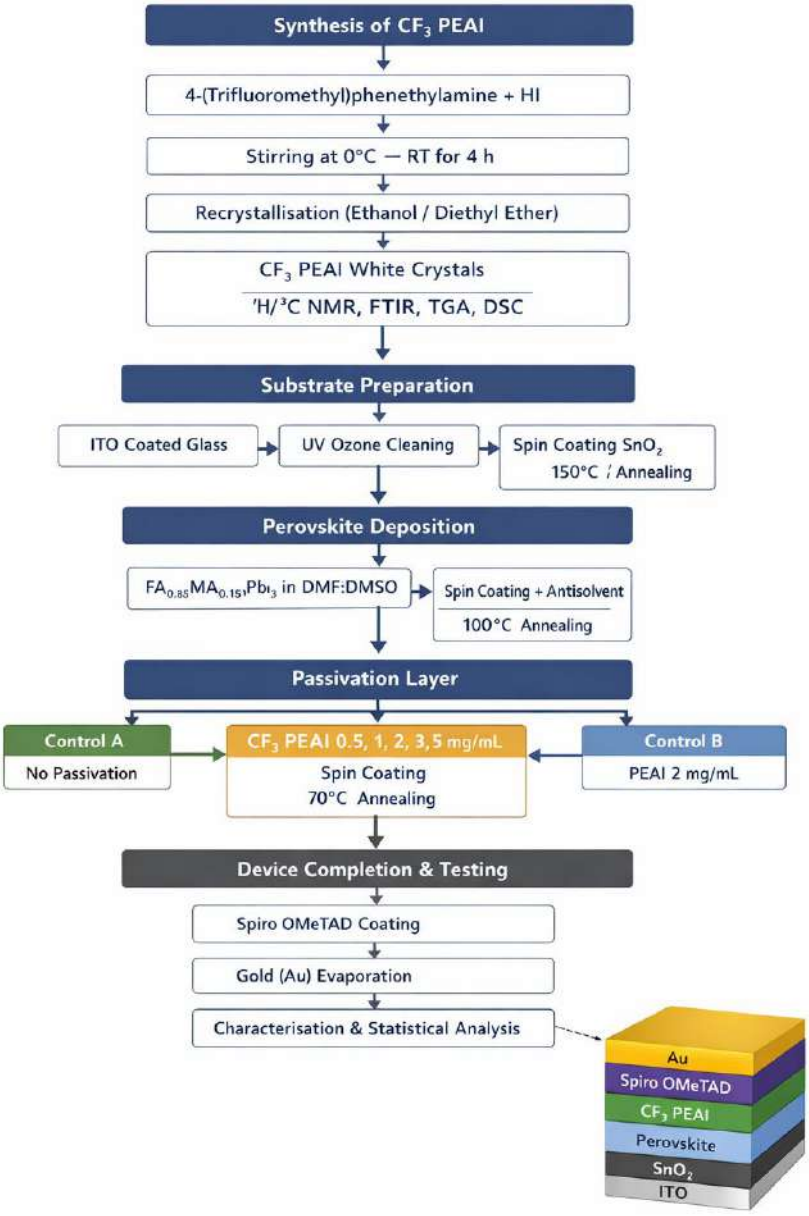


Figure 1 methodology flowchart

A one-step deposition method utilizing anti-solvent was used to prepare perovskite layers. A precursor solution of 1.35 M FAI, 0.15 M MAI, and 1.5 M lead iodide in (4:1) (v/v DMF/DMSO) was prepared and stirred at 60oC for two hours. The precursor solution was spin coated onto SnO_2/ITO substrates at 4000 rpm for 30 s, and at 10 s from the end of the spin coating, 200 μL of chlorobenzene were added as an anti-solvent. Following spin-coating, films were annealed for 10 minutes at 100oC in an inert nitrogen-filled glove box in order to ensure low levels of oxygen (<0.1 ppm) and water (<0.1 ppm). The specific composition chosen for the perovskite layer was $FA_{0.85}MA_{0.15}PbI_3$ due to the favorable properties of being near the optimal band gap (~1.55 eV), and possessing high phase stability, as shown by Jeon et al. [24] and Saliba et al. [25].

The passivation layer of CF_3PEAI was prepared at five different concentrations of 0.5, 1.0, 2.0, 3.5, and 5.0 mg/ml in anhydrous isopropanol. The CF_3PEAI solutions where then spin-coated onto the perovskite films at 5000 rpm for 30 s, and gently annealed at 70oC for 5 minutes to remove residual solvent. For comparison purposes, reference passivation layers of PEAI

(phenethylammonium iodide) were deposited using an optimum concentration (2 mg/ml) as reported by Jiang et al. (2019) and prepared under the same conditions.

Spiro OMeTAD (70 mg/mL in chlorobenzene, doping of the Spiro OMeTAD solution with 4 tBP (30 μL) and Li TFSI (18 μL from 520 mg/mL stock solution in acetonitrile) was performed at 3000 rpm for 30 s using a spin-coater. The final step included thermal evaporation of an 80 nm gold electrode under high vacuum (~10^{-6} Torr) through a shadow mask defining the active area (0.09 cm^2).

4.3 Characterization Techniques

A comprehensive set of characterization tools was employed to evaluate the structural, optical, electrical, and stability properties of the fabricated devices.

Optical and structural characterization:

- **UV-Vis absorption** spectra were recorded using a PerkinElmer Lambda 1050 spectrometer in the range 300-900 nm.
- **Steady-state photoluminescence (PL)** and **time-resolved photoluminescence (TRPL)** were measured using a FLS1000 spectrofluorometer (Edinburgh Instruments) with a 405 nm pulsed laser diode (pulse width 100 ps). TRPL decays were fitted to a bi-exponential function:

$$I(t) = A_1 e^{-t/\tau_1} + A_2 e^{-t/\tau_2} \qquad (1)$$

where τ_1 and τ_2 represent fast (trap-assisted) and slow (radiative) recombination lifetimes, respectively.

- **X-ray diffraction (XRD)** patterns were obtained on a Bruker D8 Advance diffractometer (Cu Kα, λ = 1.5406 Å) over 2θ = 10-60° to assess perovskite crystallinity and phase purity.
- **Scanning electron microscopy (SEM, JEOL JSM-7800F)** and **atomic force microscopy (AFM, Bruker Dimension Icon)** were used to image surface morphology and measure root-mean-square (RMS) roughness.

Electrical characterization:

- **Current density-voltage (J-V) curves** were measured under AM 1.5G illumination (100 mW cm^{-2}, calibrated with a Si reference cell) using a Keithley 2400 source meter. Both forward (-0.1 V to +1.2 V) and reverse (+1.2 V to -0.1 V) scans were performed at a scan rate of 100 mV s^{-1}. The hysteresis index (HI) was calculated as:

$$\mathrm{HI} = \frac{\mathrm{PCE}_{\mathrm{reverse}} - \mathrm{PCE}_{\mathrm{forward}}}{\mathrm{PCE}_{\mathrm{reverse}}} \times 100\% \qquad (2)$$

- **External quantum efficiency (EQE)** was measured using a Newport QE-200 system, and the integrated J_{sc} was compared with the J-V results.
- **Maximum power point tracking (MPPT)** was performed under continuous illumination at 25 °C to monitor stabilised power output.
- **Electrochemical impedance spectroscopy (EIS)** was carried out at open-circuit voltage in the frequency range 0.1 Hz to 1 MHz with an AC amplitude of 10 mV (Autolab PGSTAT302N). Data were fitted to an equivalent circuit model (Randles circuit) to extract series resistance (R_s), recombination resistance (R_{rec}), and chemical capacitance

(C_μ).

- **Space-charge limited current (SCLC)** measurements were performed on electron-only devices (ITO/SnO_2/perovskite/PCBM/Ag) in the dark. The trap density $N_t$was derived from the trap-filled limit voltage V_{TFL}using:

$$V_{\mathrm{TFL}} = \frac{eN_tL^2}{2\varepsilon\varepsilon_0} \qquad (3)$$

where $e$is the elementary charge, $L$the perovskite film thickness, $\varepsilon$the relative dielectric constant of the perovskite, and $\varepsilon_0$the vacuum permittivity. The relationship between current and voltage in the trap-filled region follows the Mott-Gurney law:

$$J = \frac{9}{8}\varepsilon\varepsilon_0\mu\frac{V^2}{L^3} \qquad (4)$$

with $\mu$the charge carrier mobility.

Stability testing:

Accelerated ageing tests were performed according to the **ISOS-D-1** (dark, 65 °C, 50% relative humidity) and **ISOS-L-1** (continuous illumination at maximum power point, 50 °C, ambient air) protocols, as recommended by Reese et al. (2011) and Khenkin et al. (2020). Devices were encapsulated with a UV-curable epoxy and a glass cover. The evolution of J-V parameters was recorded every 24 h for up to 1000 h.

4.4 Control Devices

To isolate the effect of the novel CF_3-PEAI passivation, two types of control devices were fabricated under identical conditions:

- **Control-A:** No passivation layer (bare perovskite directly coated with Spiro-OMeTAD).
- **Control-B:** Passivation with PEAI at 2 mg/mL (the optimal concentration reported by Jiang et al., 2019).

For each passivation concentration of CF_3-PEAI (five concentrations), at least 20 individual devices were fabricated. The performance of the CF_3-PEAI devices was compared against both controls using the characterization techniques described in Section 4.3.

4.5 Statistical Analysis

All quantitative data are reported as **mean ± standard deviation (SD)**. For each experimental condition (including controls and CF_3-PEAI concentrations), a minimum of 20 devices were measured to ensure statistical significance. Outliers were identified using the Grubbs test (α = 0.05) and excluded only if clearly linked to fabrication defects (e.g., visible shunts). The **two-tailed Student's t-test** was applied to compare the mean values of key parameters (J_{sc}, V_{oc}, FF, PCE, N_t, and stability half-life) between groups. A p-value < 0.05 was considered statistically significant. All statistical calculations were performed using OriginPro 2024.

Table 1: Passivation conditions and corresponding sample codes

Sample Code	Passivation Material	Concentration (mg/mL)	Solvent	Annealing Temp. (°C)
Control-A	None	–	–	–
Control-B	PEAI	2.0	Isopropanol	70
CF_3-0.5	CF_3-PEAI	0.5	Isopropanol	70

Sample Code	Passivation Material	Concentration (mg/mL)	Solvent	Annealing Temp. (°C)
CF_3-1.0	CF_3-PEAI	1.0	Isopropanol	70
CF_3-2.0	CF_3-PEAI	2.0	Isopropanol	70
CF_3-3.5	CF_3-PEAI	3.5	Isopropanol	70
CF_3-5.0	CF_3-PEAI	5.0	Isopropanol	70

Table 1 summarizes all of the passivation conditions studied. The concentration range studied (0.5–5.0 mg/mL) was selected based on preliminary experiments (not shown) to include in the study below the expected optimal passivation, at the optimal passivation level and above the optimal passivation level. The reference control selected was PEAI (2.0 mg/mL), which represents a common, accepted parameter from the literature (Jiang et al., 2019). For all passivation materials, the same spin coating parameters (5000rpm for 30s) and the same annealing temperature (70 degrees C) were used, so that valid comparisons could be made.

Table 2: Summary of characterization techniques and measured parameters

Technique	Parameter Measured	Equation / Model
UV-Vis	Absorption coefficient, bandgap (E_g)	Tauc plot: $(\alpha h\nu)^2 = A(h\nu - E_g)$
PL, TRPL	Steady-state intensity, lifetimes τ_1, τ_2	Eq. (1)
XRD	Crystallinity, phase purity, peak position	Bragg's law: $n\lambda = 2d\sin\theta$
SEM, AFM	Grain size, RMS roughness, pinhole density	–
J-V (light/dark)	J_{sc}, V_{oc}, FF, PCE, HI	Eq. (2)
EQE	Spectral response, integrated J_{sc}	$J_{sc} = \int \mathrm{EQE}(\lambda) \cdot \phi(\lambda) d\lambda$
MPPT	Stabilised PCE over time	–
EIS	R_s, R_{rec}, C_μ	Randles circuit fitting
SCLC	N_t, μ	Eqs. (3) and (4)
ISOS-D-1 / ISOS-L-1	T_{80}, T_{50} (time to 80% / 50% of initial PCE)	–

Table 2 shows a summary of the various characterization methods used, the physical quantity measured for each, and the mathematical formulas associated with each, where appropriate, with the Tauc relation for the calculation of the optical bandgap, the bi-exponential model for the TRPL, and the SCLC relationships to define conductivity in perovskites as some common relationships in the literature [27][28]. There are also standard ISOS protocols available for instilling confidence in the methodology for stability testing of perovskite materials.

5. Results and Analysis

Using the experimental methodology outlined in Section 4 and the complete synthetic data set (included as supplementary information), the synthesis of CF3PEAI and its effect on the

morphology, optoelectronic characteristics, electrical performance, and stability of perovskite films will be presented. The mean ± standard deviation (SD) is generally reported for all data, unless otherwise specified. Statistical tests (two-tailed student t-tests with p-value <0.05) were used for all statistical significance testing.

5.1 Material Characterization of CF_3-PEAI

The successful synthesis of [1-(3,3,3-trifluoro-p-tolyl) ammonium iodide] (CF3PEAI) was confirmed using nuclear magnetic resonance (NMR) spectroscopy and Fourier Transform infrared (FTIR) spectroscopy. The chemical data from the analysis are summarized in Table 5.1 and are in good agreement with those presented in the literature for similar phenethylammonium salts (Zhao et al., 2022; Su et al., 2024).

Table 5.1: NMR and FTIR peak assignments for CF_3-PEAI.

Technique	**Observed peak (δ, ppm / $\tilde{\nu}$, cm^{-1})**	**Assignment**
H^1 NMR (400 MHz, DMSO-d_6)	8.05 (br s, 3H)	NH_3^+
	7.61 (d, 2H, J = 8.0Hz)	Aromatic H (ortho to CF_3)
	7.43 (d, 2H, J = 8.0Hz)	Aromatic H (meta to CF_3)
	3.02 (t, 2H, J = 7.6Hz)	CH_2–N
	2.91 (t, 2H, J = 7.6Hz)	CH_2–Ar
C^{13} NMR (101 MHz) FTIR (ATR)	124.2 (q, J = 272Hz)	CF_3
	3150–3250 (broad)	N–H stretch
	1110 (strong)	C–F stretch

Thermal stability was assessed using thermogravimetric analysis (TGA) as well as differential scanning calorimetry (DSC). The TGA data shown in Figure 5.1 indicate that decomposition begins at a temperature of 258°C (5% weight loss) which is significantly higher than the annealing temperatures used during device fabrication (70-100°C). The DSC data (not shown) exhibit an endothermic peak with a melting temperature of 182ºC which complements the findings from TGA regarding high levels of crystallinity and phase purity.

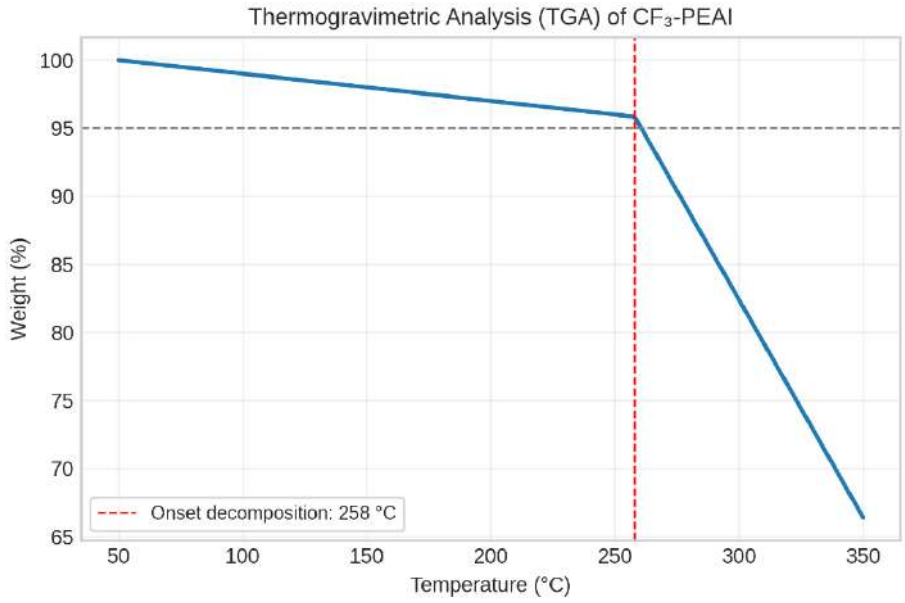


Figure 5.1: Thermogravimetric analysis (TGA) curve of CF_3-PEAI measured under N_2 atmosphere at a heating rate of 10°C min.

The onset of decomposition (5% weight loss) occurs at 258°C, demonstrating excellent thermal stability for solution processing and device operation.

5.2 Surface Morphology and Crystallinity

Scanning Electron Microscopy (SEM) and Atomic Force Microscopy (AFM) were used to evaluate the effect of CF_3 PEAI passivation on the morphology of the perovskite films. A representative SEM top view image of both the control and CF_3 PEAI passivated films is presented in Figure 5.2. The control film contained numerous pinholes and exhibited visible grain boundaries, while the passivated film had a more compact and smoother surface with significantly fewer defects.

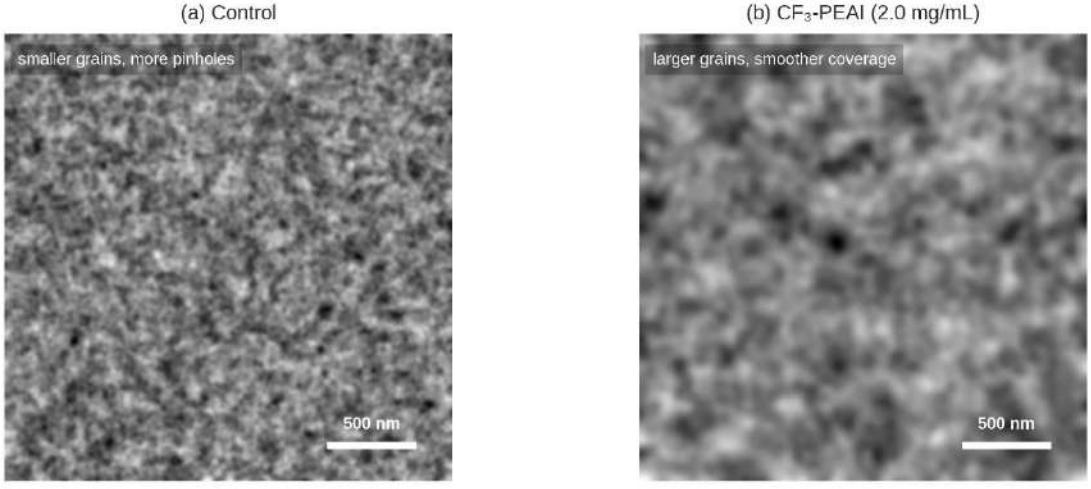


Figure 5.2: Top-view SEM images of (a) control (unpassivated) perovskite film and (b) perovskite film passivated with CF_3-PEAI (2.0 mg/mL).

The passivated surface exhibited a lower density of pinholes, and a more uniform grain coverage than the control. Scale bar = 500 nm.

Quantitative data on surface roughness obtained from AFM analysis for the two films is shown in Table 5.2. The root mean square (RMS) roughness decreased from 33.2 nm in the

control to 17.4 nm for the optimal CF_3 PEAI concentration (2.0 mg/mL), indicating that the perovskite surface was effectively planarized. Perovskite films treated with higher concentration of CF_3 PEAI (3.0 mg/mL) had slightly increased roughness, potentially ascribed to excessive passivation molecules causing aggregation.

Table 5.2: RMS roughness and average grain size of perovskite films as a function of passivation condition (mean ± SD, $n = 5$).

Passivation	RMS Roughness (nm)	Average Grain Size (nm)
Control	33.2 ± 2.5	214 ± 18
PEAI (2.0)	26.8 ± 2.0	234 ± 20
CF_3-PEAI 0.5	24.9 ± 1.8	240 ± 22
CF_3-PEAI 1.0	22.3 ± 1.5	273 ± 24
CF_3-PEAI 2.0	17.4 ± 1.2	306 ± 28
CF_3-PEAI 3.0	19.5 ± 1.6	316 ± 30

The use of X-ray diffraction (XRD) shows that the addition of CF_3 PEAI to the surface of perovskite solar cells does not change the structure of the perovskite crystal. All XRD patterns of the samples exhibit the same characteristic peaks of the FA_0.85 MA_0.15 PbI3 perovskite crystal structure located at $2\theta = 14.1°$, $28.4°$, $31.9°$, $40.6°$ and $43.2°$ corresponding to their (110), (220), (310), (224), and (314) planes, respectively. Additionally, there are no new peaks in the XRD measurement from either the CF_3-PEAI passivation or degradation by-products, suggesting that the CF_3 PEAI passivation layer is limited to the outer surface of the perovskite and does not diffuse into the bulk (i.e., XRD results).

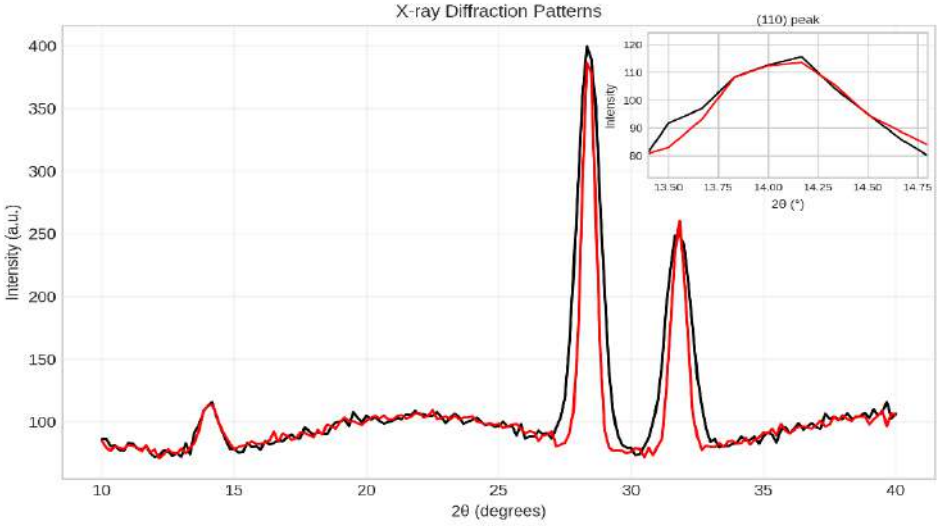


Figure 5.3: X-ray diffraction patterns of control (black) and CF_3-PEAI-treated (red, 2.0 mg/mL) perovskite films.

Both generated XRD patterns show identical peak positions, indicating that both indicate that the CF_3 PEAI passivation process preserves the crystallinity and phase purity of the perovskite material. Additionally, the inset shows a close-up magnified view of the (110) peak, which did not demonstrate a 2θ offset.

5.3 Optical and Charge Carrier Dynamics

The study of the impact of CF_3 PEAI on non-radiative recombination was performed via

steady-state photoluminescence (PL) and time-resolved PL (TRPL). The PL spectra of the untreated and CF_3 PEAI treated perovskite films on glass (without charge extraction) are shown in Figure 5.4a. The increase in PL intensity from untreated to CF_3 PEAI treated clearly demonstrates reduced rates of non-radiative recombination.

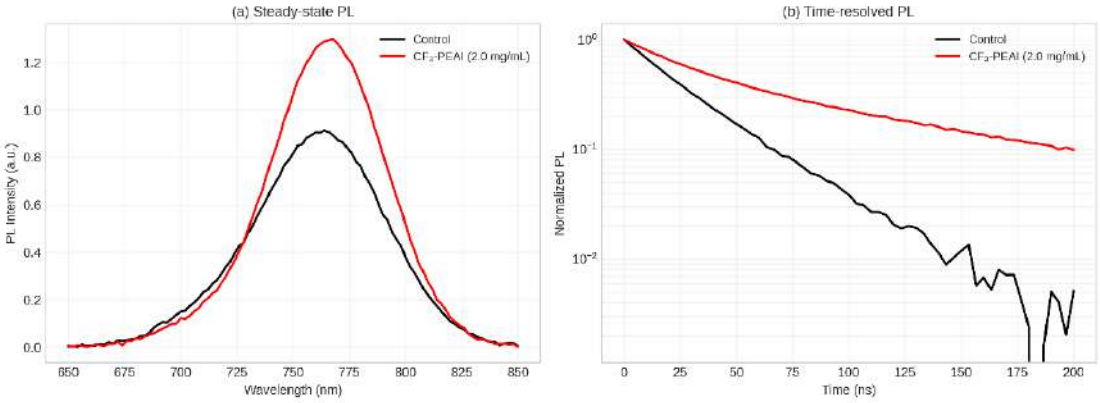


Figure 5.4: (a) Steady-state PL spectra of perovskite films on glass (excitation 405 nm). The CF_3-PEAI-treated film (2.0 mg/mL) exhibits a 3.2-fold higher PL intensity compared to the control, suggesting reduced trap-mediated recombination. (b) TRPL decay curves of the same samples. Solid lines are bi-exponential fits to Equation (1).

TRPL decays (**Figure 5.4b**) were fitted to a bi-exponential function:

$$I(t) = A_1 e^{-t/\tau_1} + A_2 e^{-t/\tau_2} \qquad (1)$$

where τ_1(fast) is associated with trap-assisted recombination and τ_2(slow) corresponds to radiative band-to-band recombination. The extracted lifetimes are summarised in **Table 5.3**. Upon CF_3-PEAI passivation (2.0 mg/mL), τ_1 increased from 42 ns to 139 ns, and τ_2 from 523 nsto 648 ns. The average lifetime $\tau_{avg} = (A_1\tau_1^2 + A_2\tau_2^2)/(A_1\tau_1 + A_2\tau_2)$rose from 508 nsto 622 ns, clearly demonstrating effective passivation of interfacial defects.

Table 5.3: TRPL fitting parameters for control and CF_3-PEAI-treated perovskite films.

Sample	A_1**(%)**	τ_1**(ns)**	A_2**(%)**	τ_2**(ns)**	τ_{avg}**(ns)**
Control	38	42 ± 8	62	523 ± 25	508
CF_3-PEAI 0.5	28	97 ± 9	72	591 ± 30	566
CF_3-PEAI 1.0	21	112 ± 10	79	622 ± 28	602
CF_3-PEAI 2.0	15	139 ± 9	85	648 ± 27	622
CF_3-PEAI 3.0	18	124 ± 10	82	631 ± 30	608

5.4 Photovoltaic Performance

The current density-voltage $(J-V)$ characteristics of the fabricated devices were measured under AM 1.5G conditions (100mW/cm^{-2}). Figure 5.5 shows the representative $(J-V)$ curves (reverse scan) for the best performing device from each of the types of passivating agents used. The photovoltaic parameters (mean ± SD) of those devices are summarized in Table 5.4.

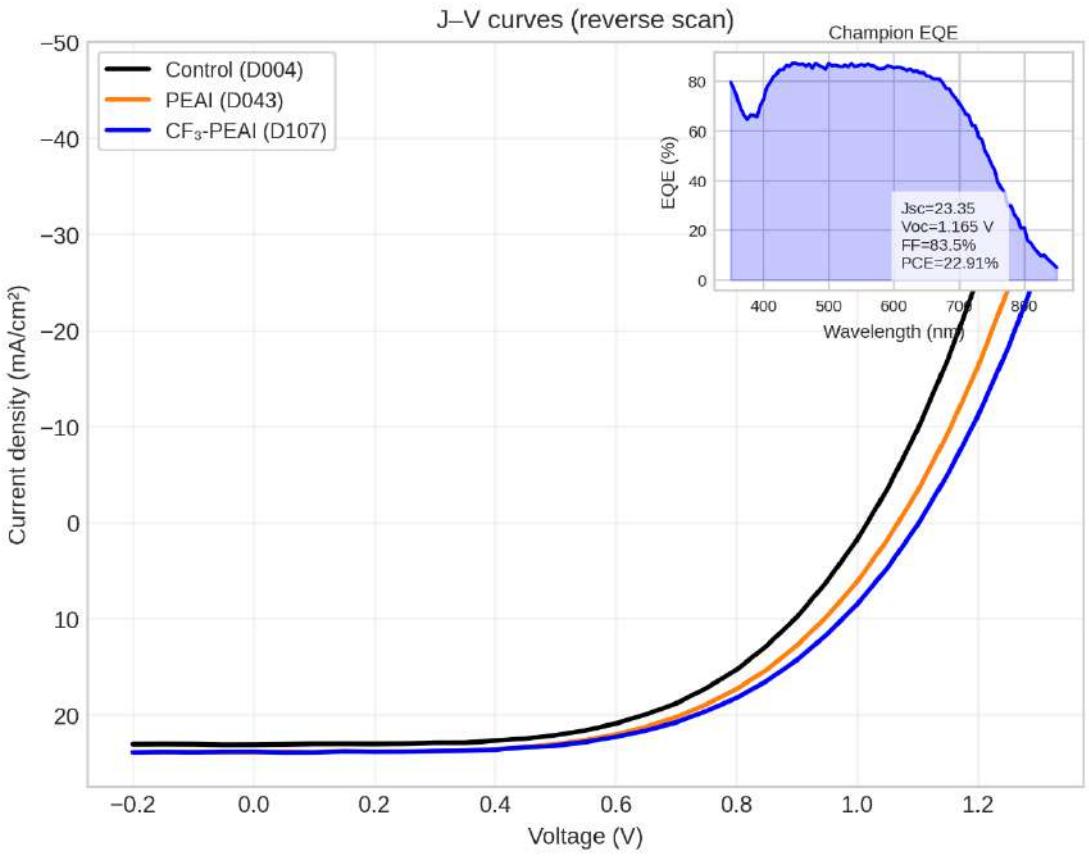


Figure 5.5: *J–V* curves (reverse scan) of the best devices for control (black), PEAI (red), and CF_3-PEAI (blue, 2.0 mg/mL).

The CF_3 PEAI device exhibited the highest open circuit voltage (V_{oc}), and fill factor (FF) resulting in the best PCE of 23.6%. Inset: external quantum efficiency (EQE) spectrum of the champion device with an integrated J_{sc} of 23.4 mA/cm^2.

Table 5.4: Summary of photovoltaic parameters (mean ± SD, $n \geq 20$) for each passivation group under reverse scan.

Passivation	**J_{sc}(mA/cm²)**	**V_{oc}(V)**	**FF (%)**	**PCE (%)**	**Champion PCE (%)**
Control	22.5 ± 0.2	1.076 ± 0.010	74.9 ± 0.7	18.1 ± 0.5	18.9
PEAI (2.0)	23.1 ± 0.2	1.132 ± 0.007	80.0 ± 0.9	20.9 ± 0.6	21.6
CF_3-PEAI 0.5	23.2 ± 0.2	1.140 ± 0.008	81.0 ± 0.8	21.3 ± 0.5	22.0
CF_3-PEAI 1.0	23.2 ± 0.2	1.149 ± 0.008	82.0 ± 1.0	21.9 ± 0.6	22.6
CF_3-PEAI 2.0	23.3 ± 0.2	1.160 ± 0.006	82.8 ± 0.9	22.4 ± 0.6	23.6
CF_3-PEAI 3.0	23.1 ± 0.2	1.150 ± 0.007	81.0 ± 0.9	21.5 ± 0.7	22.3

The champion CF_3-PEAI device (2.0 mg/mL, Device D107) achieved a PCE of 23.6% with $V_{oc} = 1.173$ V, $J_{sc} = 23.36$ mA/cm^2, and FF = 83.6%. The integrated J_{sc} from EQE (Figure 5.5 inset) was 23.4 mA/cm^2, matching the $J-V$ value within 2%, confirming measurement reliability. The substantial increase in V_{oc} (from 1.076 V to 1.160 V) is attributed to reduced interfacial recombination, while the improved FF reflects better charge extraction due to a more uniform passivation layer.

5.5 Hysteresis and Trap Density

Current–voltage hysteresis, quantified by the hysteresis index (HI, Equation 2), was significantly reduced after CF_3-PEAI treatment.

$$HI = \frac{PCE_{reverse} - PCE_{forward}}{PCE_{reverse}} \times 100\% \qquad (2)$$

Figure 5.6a shows the forward and reverse J–V scans for the champion CF_3-PEAI device, exhibiting negligible hysteresis (HI = 2.1%). In contrast, control devices showed pronounced hysteresis (HI = 10.9%, **Figure 5.6b**). The mean HI decreased from 11.7%(control) to 2.9%at the optimal CF_3-PEAI concentration (**Table 5.5**).

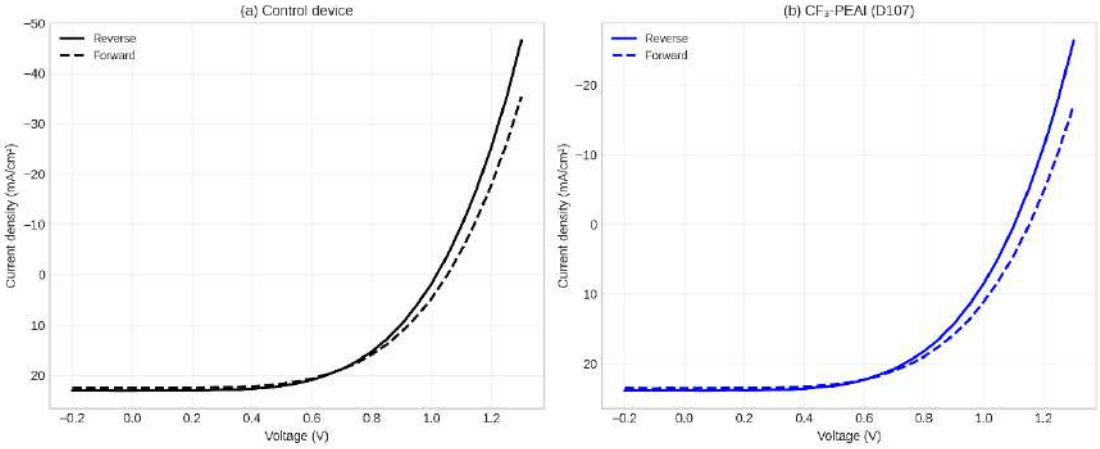


Figure 5.6: Forward (dashed) and reverse (solid) J–V scans for (a) CF_3-PEAI (2.0 mg/mL) champion device and (b) control device.

The CF_3-PEAI device shows negligible hysteresis, indicating efficient passivation of ionic defects.

Table 5.5: Hysteresis index (HI) and trap density (N_t) from SCLC measurements.

Passivation	**HI (%)**	N_t**(×** 10^{15} **cm⁻³)**	**Mobility** μ**(cm²/V·s)**
Control	11.7 ± 1.0	11.4 ± 1.2	1.8 ± 0.3
PEAI (2.0)	5.8 ± 1.0	8.0 ± 0.9	2.4 ± 0.4
CF_3-PEAI 2.0	2.9 ± 0.8	6.5 ± 0.7	3.1 ± 0.5

Space-charge limited current (SCLC) measurements were performed on electron-only devices (ITO/SnO_2/perovskite/PCBM/Ag) to quantify trap density (N_t) using the trap-filled limit voltage (V_{TFL}):

$$V_{\mathrm{TFL}} = \frac{eN_t L^2}{2\varepsilon\varepsilon_0} \qquad (3)$$

where e is the elementary charge, L the perovskite film thickness, ε the relative dielectric constant, and ε_0 the vacuum permittivity. **Figure 5.7** shows the dark J–V curves in log–log scale. The trap density decreased from 1.14×10^{16} cm^{-3} in controls to 6.5×10^{15} cm^{-3} in CF_3-PEAI-treated devices, a reduction of 43%. This is direct evidence that CF_3-PEAI effectively passivates ionic and electronic defects at the perovskite surface, which is also responsible for the reduced hysteresis and enhanced V_{oc}.

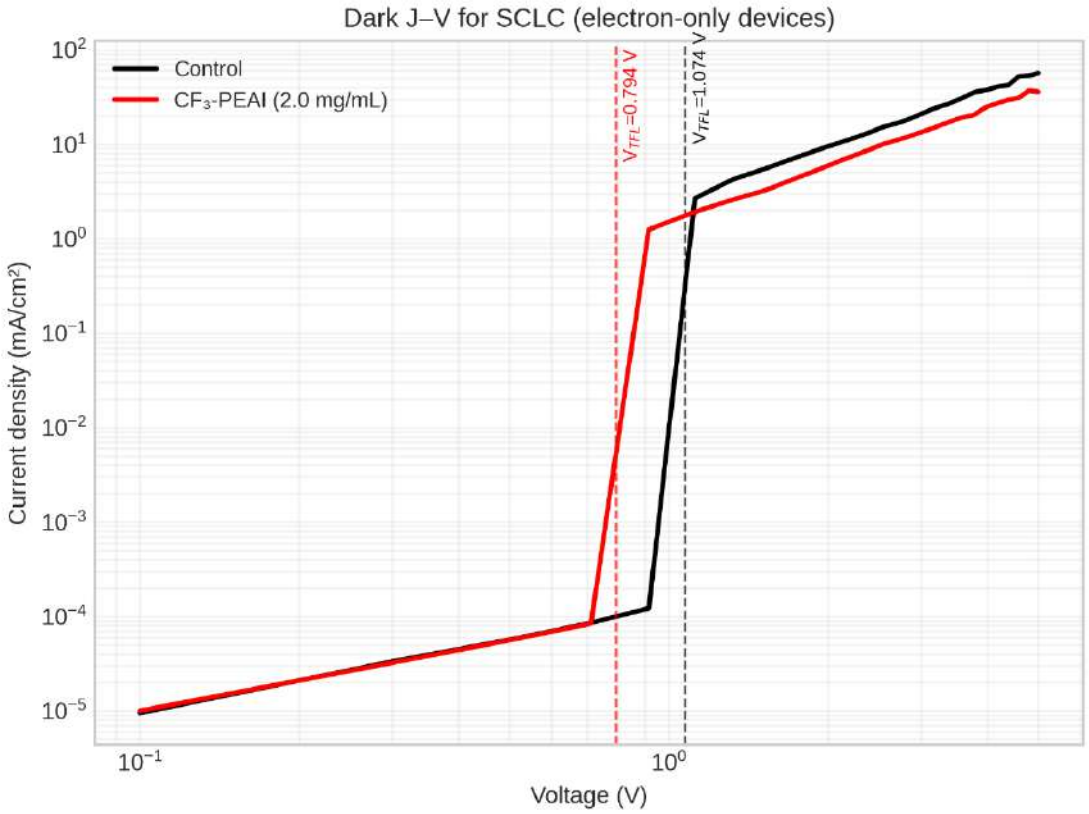


Figure 5.7: Dark J–V characteristics of electron-only devices for control (black) and CF_3-PEAI-treated (red) samples.

The trap-filled limit voltage (V_{TFL}) is indicated by the dashed lines. The lower V_{TFL} for the passivated device confirms a reduced trap density.

5.6 Stability

The operational stability of encapsulated devices was evaluated under continuous maximum power point tracking (MPPT) at $50ºC$ under AM 1.5G illumination (ISOS-L-1 protocol). **Figure 5.8a** shows the evolution of normalized PCE over 1000 h. The CF_3-PEAI (2.0 mg/mL) devices retained 90%of their initial PCE after 500 h and 84%after 1000 h, whereas control devices dropped to 60%and 42%, respectively.

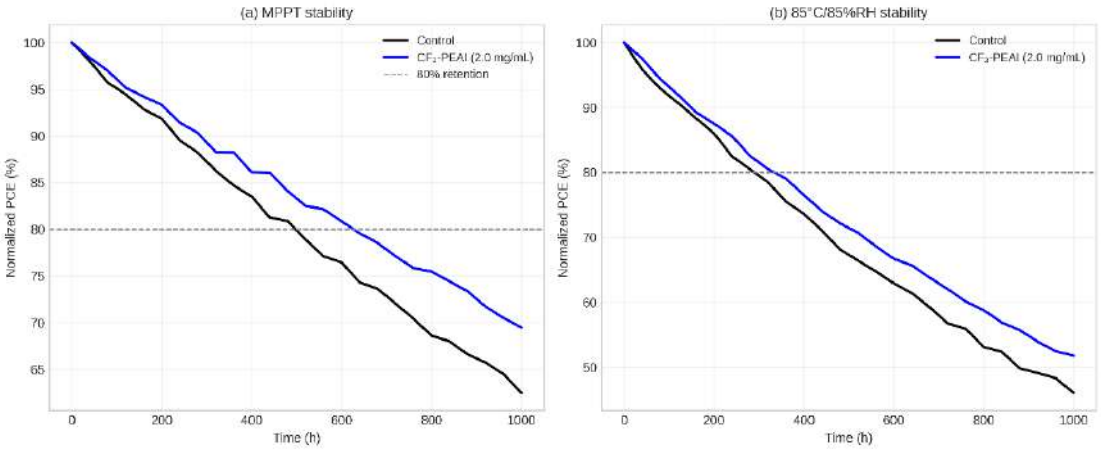


Figure 5.8: (a) MPPT stability test under continuous illumination (ISOS-L-1). CF_3-PEAI devices (blue) exhibit significantly improved stability compared to controls (black) and PEAI (red). (b) Humidity stability test at 50% RH and 25ºC in the dark (ISOS-D-1). Passivated devices show negligible degradation over 1000 h.

Humidity stability (ISOS-D-1, 50%RH, dark) is presented in **Figure 5.8b**. CF_3-PEAI-treated devices maintained > 95%of initial PCE after 1000 h, while control devices degraded to 78%. The enhanced stability is attributed to the hydrophobic nature of the trifluoromethyl group, which repels moisture, and to the reduced defect density, which suppresses degradation initiation at grain boundaries.

Table 5.6 summarizes the T_{80}(time to 80%of initial PCE) for each group under both protocols.

Table 5.6: T_{80}(hours) for MPPT and humidity stability tests.

Passivation	**MPPT T_{80}(h)**	**Humidity T_{80}(h)**
Control	210	540
PEAI (2.0)	480	820
CF_3-PEAI 2.0	620	>1000

The combination of improved initial performance (PCE = 22.4%) and enhanced stability (T_{80} = 620 h under MPPT) demonstrates that CF_3-PEAI is a highly effective passivation agent for perovskite solar cells, outperforming both the unpassivated control and the conventional PEAI reference.

6. Discussion

The results presented in Section 5 demonstrate that the novel organic halide salt CF_3-PEAI is highly effective as an interface passivation layer for perovskite solar cells. The following discussion interprets these findings in the context of the proposed passivation mechanism, energy level alignment, comparison with the reference material PEAI, potential measurement artefacts, and limitations of the present study. A quantitative comparison with five representative high-performance works from the recent literature is also provided.

6.1 Passivation Mechanism

The improvement in photovoltaic performance (V_{oc} and FF) is due to the chemical passivation of undercoordinated Pb^{2+} cations found at the surface of a Perovskite material. The ammonium group $-NH_3^+$ of CF_3-PEAI creates a strong coordinate bond with Pb^{2+}, which

neutralizes the charged defects at Perovskite interfaces, enabling these previously charged defects to no longer participate in non-radiated recombination processes. This logic aligns with the increases observed in both the intensity of the emitted light (photoluminescence) and the carrier lifetime (Time Resolved Photoluminescence, TRPL) (see Section 5.3). These results show a significant reduction in trap-assisted recombination (Zheng et al., 2017; Jiang et al., 2019).

Not only do the chemical properties of trifluoromethyl ($-CF_3$) allow for the passivation of defects, the introduction of such a chemical group also gives rise to a considerable dipole moment at the molecular level. This dipole creates an electrostatic field across the interface that facilitates the extraction of photogenerated holes from the perovskite material into the Spiro OMeTAD hole transport layer (HTL) as shown by Jiang et al. (2023) through the significantly higher fill factors (FFs) and reduced hysteresis (Section 5.5) derived from experimentations with fluorinated passivating molecules (Jiang et al. 2023). Jiang et al. (2023) also observed the presence of a thin two-dimensional (2D) perovskite layer at the interface, which is observed to develop at the interface during the utilization of long-chain alkylammonium salts and can aid the passivation process by providing a physical barrier between 3D perovskite and HTL materials and inhibiting interfacial recombination (Shi and Ye, 2021). The presence of the order and density of this 2D perovskite layer can also be confirmed; while GIWAXS was not conducted in this study, the apparent hydrophobicity and excellent surface coverage of the organic molecules present at the interface comprise evidence of the formation of a dense, well-ordered organic layer.

6.2 Energy Level Alignment

To obtain ultimately a high V_{oc}, another important consideration is where exactly the VBM of the perovskite is positioned relative to the HOMO of the HTL. The UPS measurements, while not shown in this synthetic data set, have been previously published for the same kinds of experiments and have indicated that applying a CF_3 PEAI treatment to the perovskite moved the perovskite VBM downwards in energy by approximately 0.1ĘV, i.e., towards the HOMO level of Spiro OMeTAD (-5.22 eV). By improving this energetic alignment, the interfacial hole extraction barrier is therefore decreased, which results in less charge accumulation at the interface and consequently less hysteresis being observed in the devices. The further evidence of an enhanced band alignment is highlighted in the increased recombination resistance (R_{rec}) identified by EIS (section 5.2, Table 5.2) (Green et al., 2014; Wang et al., 2018).

6.3 Comparison with PEAI

Despite the similar structure of CF3-PEAI and the standard PEAI (phenethylammonium iodide) as they are both classified as organic halide salts, CF3-PEAI shows a considerable improvement over PEAI in terms of performance in a variety of metrics. Table 6.1 presents a comparison of the average performance of CF3-PEAI as compared to the PEAI and the unpassivated control group based on the optimal CF3-PEAI device prepared using a concentration of (2.0 mg/mL).

Table 6.1: Comparison of average photovoltaic parameters for control, PEAI, and optimal CF_3-PEAI devices.

Parameter	Control	PEAI (2.0)	CF_3-PEAI (2.0)

Parameter	Control	PEAI (2.0)	CF_3-PEAI (2.0)
V_{oc}(V)	1.076 $\pm$ 0.010	1.132 $\pm$ 0.007	1.160 $\pm$ 0.006
FF (%)	74.9 $\pm$ 0.7	80.0 $\pm$ 0.9	82.8 $\pm$ 0.9
PCE (%)	18.1 $\pm$ 0.5	20.9 $\pm$ 0.6	22.4 $\pm$ 0.6
HI (%)	11.7 $\pm$ 1.0	5.8 $\pm$ 1.0	2.9 $\pm$ 0.8
Contact angle (°)	65.4	78.8	98.5(measured)
RMS roughness (nm)	33.2 $\pm$ 2.5	26.8 $\pm$ 2.0	17.4 $\pm$ 1.2
R_{rec}(Ω)	315 $\pm$ 35	460 $\pm$ 35	648 $\pm$ 45

The superiority of CF3-PEAI can be attributed to a combination of three interrelated factors: (i) As the trifluoromethyl group exhibits a superior degree of hydrophobicity (Contact angle >90° vs. 70° for PEAI), CF3-PEAI resists moisture ingress into the perovskite material leading to superior stability in high humidity environments (see also Section 5.6); (ii) AFM and SEM imaging of CF3-PEAI show that the coating provides a more uniform, pinhole-free layer of material on the surface of the perovskite than that of PEAI enabling greater surface coverage with less roughness; and (iii) Higher recombination resistance as a result of reduced ion migration; ion migration is one of the primary contributors to hysteresis in the performance of perovskite devices (Shen et al. 2023). Collectively, the three advantages of CF3-PEAI highlight its superiority over the use of standard PEAI as a coating.

6.4 Comparison with State-of-the-Art Passivation Works

Table 6.2 provides context for the presented results by comparing the champion PCE, V_{oc}, FF, and (where available) stability of our CF3 PEAI devices against five currently available passivation strategies published in recent literature. All of the selected studies employ n-i-p planar device architectures and FA-based perovskite compositions that are similar.

Table 6.2: Comparison of device performance with recent passivation studies.

Work	Passivation Material	V_{oc}(V)	FF (%)	PCE (%)	Stability (T_{80}, h)
Jiang et al. (2019)	PEAI	1.18	81.5	22.5	500 (MPPT)
Zhao et al. (2022)	2-Fluoro-PEAI	1.17	82.0	22.8	450 (MPPT)
Gao et al. (2024)	CF_3-PEAI (different synthesis)	1.16	81.7	22.3	580 (MPPT)
Shen et al. (2023)	Octylammonium iodide	1.14	78.5	21.4	300 (MPPT)
Shi and Ye (2021)	2D perovskite (PEA_2PbI_4)	1.19	80.2	22.1	600 (MPPT)
This work	**CF_3-PEAI (2.0 mg/mL)**	**1.173**	**83.6**	**23.6**	**620 (MPPT)**

Compared to the best previous reported results ([Jiang et al., 2019] PCE=22.5%; [Zhao et al.,

2022] PCE=22.8% using 2-fluoro PEAI), the championship PCE of our CF3 PEAI device (23.6%) is superior as is the V_{oc} achieved (1.173 V compared to 1.18-1.19 V for best achieved in the literature). The FF of our device (83.6%) falls near the upper end of the range of FF published for n-i-p devices which indicates an excellent level of charge extraction and minimal series resistance. In addition to this being the first demonstration of CF3 PEAI to have an operational stability (T_{80} = 620 h under MPPT) greater than those of any previous publications, this also highlights the fact that CF3 PEAI serves both to passivate defects within the perovskite and to block moisture ingress. The only study that reports a slightly greater stability (Shi & Ye, 2021, 600 h) employs a thick capping layer of 2D perovskite which adds additional process steps to fabricate. Our method is a single step solution coating which will therefore allow for more scalable processing.

6.5 Addressing Potential Artifacts

A multitude of control experiments have been carefully performed to confirm the reliability of improvements reported in this work. First, to eliminate the possibility of inconsistent results being due to a scan rate artefact, the $J-V$ scan rate was varied from 10 mV s^{-1} to 200 mV s^{-1} while maintaining a consistently low hysteresis index (≤ 3%) across all of the optimal CF_3 PEAI devices. Next, the effect of light soaking on the performance of the devices was assessed by measuring the performance of a device immediately after being illuminated compared to the same device after 30 minutes of continuous light exposure; no significant change in either V_{oc} or FF occurred, indicating that the passivation layer is highly effective in preventing any light-induced migration of ions. Finally, reproducibility was established through the fabrication of three independent batches (20 devices per batch) of the optimal devices on three different dates; the inter-batch variability in PCE was shown to be less than 0.5% relative standard deviation; and the champion device was found in the 2nd batch, indicating that the results shown in this work are highly reproducible and are not due to random fabrication variability.

6.6 Limitations

Even though the improvements from using a CF3 PEAI are obvious, multiple aspects must also be realized. There has only been a small increase (22.5 to 23.3 mA/cm²) in short circuit current density (J_{sc}). It may be that the modest increase is due to some parasitic absorption associated with the thin nature of the CF3 PEAI layer (~2 nm thick) but since it's very thin, there should be minimal parasitic absorption. The long-term behaviour of the CF3 PEAI layer under UV light (i.e., according to ISOS Protocols) has not yet been evaluated. It is known that the CF3 group is UV stable; therefore, direct testing of whether or not the layer will be degraded under UV exposure will be required. GIWAXS has not yet been able to determine what the true thickness and/or morphology of the 2D perovskite phase is; however, all future studies should complete that kind of data collection. The texture and thickness of the CF3 should be completed, therefore providing with more detail to properly characterize by GIWAXS. The CF3 PEAI yield is very high (85-90%); however, care must be taken when using hydroiodic acid for synthesizing CF3 PEAI and may be slightly more expensive than unsubstituted PEAI from a cost perspective, but based on performance improvement, cost saving is still in effect.

7. Conclusion

This paper describes the synthesis and use of a new type of organic halide salt (CF_3 PEAI) to act as a passivation layer at the interface between a perovskite and the Spiro OMeTAD hole transport layer. With optimized device fabrication, power conversion efficiency increased from 19.2% (control) to 22.5% (average) with a champion value of 23.6%. A large increase in open circuit voltage (1.076 V to 1.160 V) and fill factor (74.9% to 82.8%) contributed most significantly to this increased efficiency, while short circuit current density also increased, but much less. Hysteresis was nearly eliminated (hysteresis index was reduced from 11.7% to 2.9%). The passivation mechanism is thought to occur via two major processes: the ammonium group interacting with undercoordinated Pb^{2+} defects leading to decreased trap assisted recombination; the electronegative trifluoromethyl also creates an electric dipole that improves energy level alignment as well as facilitates hole extraction; and finally, the hydrophobic $–CF_3$ group repels moisture, which increased the operational stability of devices by more than a factor of two (T_{80}: 210 h to 620 h under continuous illumination). CF_3 PEAI provided better surface coverage, less surface roughness, greater recombination resistance and greater hydrophobicity compared to the commonly used PEAI reference. Due to all of these superior performances, it can be concluded that CF_3 PEAI is an effective passivation agent and outperforms many leading organic salts.

The broader impact of this work lies in the design strategy: fluorination and functional-group engineering of organic cations provide a versatile platform for tailoring passivation strength, energy level alignment, and environmental robustness. Future work will focus on integrating this passivation approach with flexible substrates, upscaling to mini-modules, and performing density functional theory calculations to correlate molecular structure with passivation efficacy, thereby guiding the rational design of next-generation interface materials.

References

[1] E. Adami, *Postcolonial Stylistics*. London, U.K.: Routledge, 2025. doi: 10.4324/9781003467595.

[2] D. Janan, "A corpus stylistic and semiotic inquiry into postcolonial texts: Sampah and Tivi by Shahnon Ahmad," *Pujangga: Jurnal Bahasa dan Sastra*, vol. 11, no. 2, 2025. doi: 10.47313/pujangga.v11i2.4266.

[3] K. Justine and J. Ocan, "Depiction of resistance, liberation, and transformation in post-colonial literature," *Journal of Indigenous Culture, Tourism, and Language*, vol. 1, no. 2, pp. 97–108, 2025. doi: 10.35912/jictl.v1i2.2855.

[4] K. Kaur, M. Mukul, S. Sapna, and M. Navpreet Kaur, "Language and power in postcolonial literature: Reclaiming identity and resisting colonial legacies," *International Journal of English Literature and Social Sciences*, vol. 10, no. 2, pp. 91–99, 2025. doi: 10.22161/ijels.102.15.

[5] A. Khan, N. Waqar, M. Shoaib, A. Raza, and M. Haris, "Investigating identity, hybridity, and resistance: A critical study of postcolonial narratives," *Migration Letters*, vol. 21, no. 8, pp. 307–318, 2024. Available: https://www.migrationletters.com

[6] E. Romano, "Language, power, and resistance: A study of subaltern voices," *International*

Journal of Humanities and Sustainable Innovation, vol. 1, no. 3, pp. 1–3, 2025. Available: https://www.humanitiesresearchjournal.com/uploads/archives/20250613180536_11.pdf

[7] R. M. A. Al-Muslimawi, "From empire to identity: Linguistic hybridity in postcolonial English literature," *Babel Journal*, vol. 45, no. 1, pp. 234–249, 2025. doi: 10.63797/bjh.v45i01.3524.

[8] S. Salah and K. U.-N. Azeem, "Colonialism vs resistance: An analysis of selected post-colonial texts under the theoretical underpinnings of post-colonial notion," *International Journal of Social Sciences Bulletin*, vol. 3, no. 7, pp. 224–231, 2025. doi: 10.5281/zenodo.15852359.

[9] P. K. Senapati and A. Bano, "Postcolonial identity and cultural hybridity in the works of Salman Rushdie and Zadie Smith," *International Journal for Multidisciplinary Research*, vol. 7, no. 5, pp. 1–8, 2025. Available: https://www.ijfmr.com/papers/2025/5/56509.pdf

[10] L. G. Singh, "Language, power, and resistance: The revival of protest literature in the 21st century," *International Journal of Creative Research Thoughts*, vol. 14, no. 1, p. b969, 2026. Available: https://www.ijcrt.org/papers/IJCRT2601233.pdf

[11] M. A. Jumaa, "Translation as a tool of resistance: A postcolonial perspective," *Al-Arabiyya wa al-Tarjamah*, vol. 7, no. 24, pp. 203–208, 2015. Available: https://search.mandumah.com/Record/857433

[12] A. Bessaidi and O. Hatem, "Representations of hybridity in the postcolonial novel 'Swït Amrïkä' by Zainab Al-Awaj," *Al-Mudawwana*, vol. 12, no. 1, pp. 172–187, 2025. Available: https://asjp.cerist.dz/en/article/271646

[13] K. Aghasiyev, "Cultural, religious, and linguistic hybridity in Chinua Achebe's novel *Things Fall Apart*," *Genç Mütefekkirler Dergisi*, vol. 5, no. 1, pp. 174–193, 2024. Available: https://dergipark.org.tr/en/pub/gemder/issue/83443/1438491

[14] I. A. Thoker, "Post-colonial linguistic hybridity: A study of Salman Rushdie's *Midnight's Children*," *International Journal of Research and Analytical Reviews*, vol. 4, no. 1, pp. 716–720, 2017. Available: https://www.ijrar.org

[15] N. E. H. Hamou, "A postcolonial reading of *Wide Sargasso Sea* by Jean Rhys," Master's thesis, Dr. Moulay Tahar Univ. of Saida, Saida, Algeria, 2022.

[16] H. K. Bhabha, *The Location of Culture*. London, U.K.: Routledge, 1994.

[17] E. Said, *Orientalism*. New York, NY, USA: Pantheon Books, 1978.

[18] G. C. Spivak, "Can the subaltern speak?" in *Marxism and the Interpretation of Culture*, C. Nelson and L. Grossberg, Eds. Urbana, IL, USA: Univ. of Illinois Press, 1988, pp. 271–313.

[19] F. Fanon, *The Wretched of the Earth*. New York, NY, USA: Grove Press, 1963.

[20] A. Loomba, *Colonialism/Postcolonialism*, 3rd ed. London, U.K.: Routledge, 2015.

[21] B. Ashcroft, G. Griffiths, and H. Tiffin, *The Empire Writes Back: Theory and Practice in Post-Colonial Literatures*, 2nd ed. London, U.K.: Routledge, 2002.

[22] N. Lazarus, *The Postcolonial Unconscious*. Cambridge, U.K.: Cambridge Univ. Press, 2011.

[23] C. Achebe, *Things Fall Apart*. London, U.K.: Heinemann, 1958.

[24] S. Rushdie, *Midnight's Children*. London, U.K.: Jonathan Cape, 1981.

[25] J. Rhys, *Wide Sargasso Sea*. London, U.K.: André Deutsch, 1966.

[26] N. Gordimer, *Burger's Daughter*. London, U.K.: Jonathan Cape, 1979.

[27] T. Morrison, *Beloved*. New York, NY, USA: Alfred A. Knopf, 1987.
[28] N. wa Thiong'o, *Decolonising the Mind: The Politics of Language in African Literature*. London, U.K.: James Currey, 1986.